



## ARTICLE

Received 00th January 20xx,

**Collective motion of self-propelled chemical garden tubes**

Accepted 00th January 20xx

Pawan Kumar,<sup>a,b</sup> Qingpu Wang,<sup>a</sup> Dezső Horváth,<sup>c</sup> Ágota Tóth<sup>b</sup> and Oliver Steinbock<sup>a,†</sup>

DOI: 10.1039/x0xx00000x

In H<sub>2</sub>O<sub>2</sub> solutions, manganese-containing chemical garden tubes can self-propel due to the catalytic production and ejection of oxygen bubbles. Here, we investigate the collective behavior of these self-assembled precipitate tubes. In thin solution layers, the tubes show definite autonomous dynamics with only weak interactions that result from fluid motion around the moving units and directional changes during collisions. In thick solution layers with convex menisci forcing spatial confinement, the tubes undergo cycles of self-assembly and dispersion. This collective motion results from the rhythmic creation of a large master bubble around which the tubes align tangentially.

**1. Introduction**

For centuries, the complex shapes and striking colors of chemical gardens have attracted the interest of scientists and laymen alike. Chemical gardens consist of vertical tubes and nodules that can reach lengths of several centimeters<sup>1</sup> within a few seconds or minutes, making them attractive demonstration experiments. In the classic version of the experiment, small salt grains are seeded into a sodium silicate solution.<sup>2</sup> The salt dissolution within the alkaline solution induces the formation of insoluble products that surround the seed as a semipermeable membrane. Osmotic pressure quickly breaches the membrane and creates an osmotic pump, ejecting buoyant salt solution from the membrane-bound seed. Tubular precipitates, such as metal hydroxide and silica, then grow at the interface between the rising jet and the surrounding silicate solution to constitute the chemical garden.

Contemporary research has identified several other growth regimes<sup>3,4</sup>, quantified the underlying dynamics<sup>5</sup>, and greatly expanded the range of product materials to include insoluble metal sulfides<sup>6</sup>, carbonates<sup>7</sup>, phosphates<sup>8-9</sup> as well as polyoxometalates<sup>10,11</sup>, and even hydrogels<sup>12</sup>. Furthermore, technical applications are being explored as inexpensive absorbent/catalytic materials to fight chemical spills<sup>13</sup>, sensor-

platforms for microfluidics<sup>14</sup>, and biomimetic scaffolds for the growth of osteoblasts<sup>15</sup>. In the context of hydrothermal vents in the deep ocean, chemical garden precipitates are a porous model material for the study of prebiotic processes and possibly linked to the origins-of-life.<sup>16</sup> The precipitate membranes also have ion-specific permeabilities and can sustain electric voltages for long periods of time.<sup>17</sup>

Very recently, Mn-based chemical gardens were shown to undergo self-propulsion in H<sub>2</sub>O<sub>2</sub> solutions.<sup>18</sup> This active motion results from the catalytic decomposition of peroxide within the cavity of the precipitate tube and the subsequent ejection of small oxygen bubbles. Similar microrockets had previously been synthesized via the roll-up of thin layers formed by physical vapor deposition<sup>19,20</sup> or specialized electrochemical methods.<sup>21-23</sup> The simplicity of the chemical-garden growth, however, provides an inexpensive and scalable methodology that widens the repertoire of accessible materials and shapes. For example, two of us recently demonstrated the production of branched T-shaped tubes as well as the shape-preserving chemical conversion of CaCO<sub>3</sub> tubes.<sup>24</sup>

Here, we describe experimental results on the collective motion of Mn-based chemical garden motors. In general, the motion of interacting units can create distinct patterns and dynamics as exemplified by bioconvection<sup>25</sup>, pulsating clouds of insects<sup>26</sup>, flocks of birds<sup>27</sup>, and streams of pedestrians<sup>28</sup>. Similar swarming patterns have been observed for synthetic systems, such self-propelled nano- and micro-units. For instance, Ibele et al.<sup>29</sup> reported the fast movement of AgCl particles under UV illumination by self-diffusiophoresis along with schooling-like clustering of particles. More recent work brought the concept of swarming synthetic units closer to applications as exemplified by multitudes of functionalized nanoparticles repairing broken microcircuits.<sup>30</sup> Clearly the conjunction of self-propulsion and emergent collective

<sup>a</sup> Florida State University, Department of Chemistry and Biochemistry, Tallahassee, FL 32306-4390, USA.

<sup>b</sup> Department of Physical Chemistry and Materials Science, University of Szeged, Rerrich Béla tér 1, Szeged H-6720 Hungary.

<sup>c</sup> Department of Applied and Environmental Chemistry, University of Szeged, Rerrich Béla tér 1, Szeged H-6720 Hungary.

† Email: osteinbock@fsu.edu.

Electronic Supplementary Information (ESI) available: [details of any supplementary information available should be included here]. See DOI: 10.1039/x0xx00000x

behavior is a vast research field that—despite its potential for scientific and engineering discoveries—remains widely unexplored. Our work contributes to this exploration by demonstrating collective behavior of chemically self-propelling units that are inexpensive and easy to produce. It also contributes detailed results on rhythmic self-assembly that is dominated by reaction-induced gas bubbles.

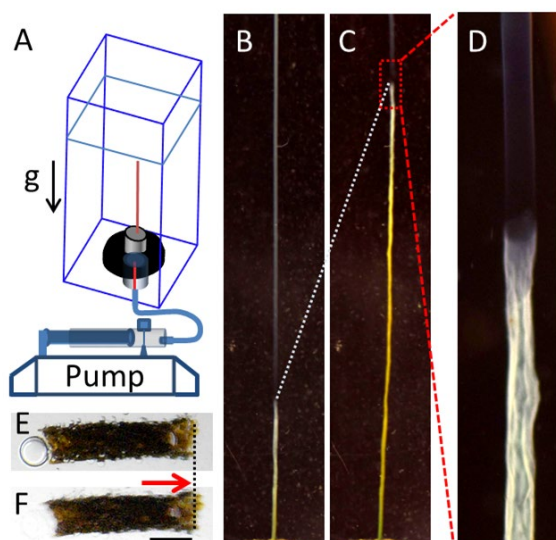


**Fig. 1** (Color online). (A) Schematic diagram of the flow-controlled synthesis system. Resulting tubular precipitates at (B) 18 s and (C) 84 s after the start of solution injection (field of view:  $1.2 \times 7.5 \text{ cm}^2$ ). (D) Close-up ( $1.6 \times 8.2 \text{ mm}^2$ ) of the growing tube tip. In  $\text{H}_2\text{O}_2$  solution, a short segment of a chemical garden tube (E) ejects an oxygen bubble causing self-propulsion just underneath the air-water interface in the direction of the arrow. The resulting position is shown in (F) with the dotted line highlighting the small spatial advance.

## Experiment

Tube production followed a method described in an earlier study that also characterized the product material.<sup>18</sup> It utilized analytical chemical reagents, specifically  $\text{MnCl}_2$  (BTC Beantown Chemicals, anhydrous 97 %),  $\text{CuSO}_4 \cdot 5\text{H}_2\text{O}$  (VWR Chemicals), and  $\text{Na}_2\text{SiO}_3 \cdot 5\text{H}_2\text{O}$  (Fisher Chemicals). All the solutions were prepared with nanopure water filtered using a Barnstead Easypure UV system. To grow the precipitate tube, a Plexiglass reactor ( $2.5 \times 2.5 \times 11.7 \text{ cm}^3$ ) was filled with 50 mL of 1.0 M  $\text{Na}_2\text{SiO}_3$  solution. The salt solution (0.4 M  $\text{MnCl}_2$  and 0.1 M  $\text{CuSO}_4$ ) was injected into the reservoir in the upward direction through a glass capillary (inner diameter 1 mm) at a constant flow rate of 8 mL/h using a syringe pump (New Era Pump Systems, NE-4000). The resulting chemical garden tubes grew vertically at a constant speed of  $0.60 \pm 0.03 \text{ cm s}^{-1}$  with an average outer diameter of  $0.44 \pm 0.02 \text{ mm}$  (see Figs. 1B and 1C). A closer inspection of the tube tip, Fig. 1D, reveals the hollow structure separating the injected solution from the outer silicate solution. Interestingly, the color of the tube

varies from a bright blue near the tip to a brownish yellow below. When the tube touched the upper surface of silicate solution, the pump injection was stopped and the precipitate tube was transferred from the reactor into a Petri dish to be rinsed and kept in nanopure water.

For the self-motion experiments, we cut the precipitate tubes into small fragments (length  $\approx 2.0 \text{ mm}$ ) using a razor blade. The cut structures were then submerged in  $\text{H}_2\text{O}_2$  solutions of various concentrations (2 to 10% w/v) which were prepared from the original 30%  $\text{H}_2\text{O}_2$  (VWR Chemicals and Macron Fine Chemicals). We studied two different experimental systems, of which only one gave rise to large bubbles and strong collective motion. The first system, Fig. 2A, was created by slowly spreading 4 mL hydrogen peroxide solution on a clean polystyrene Petri dish surface using a pipette. As we will describe in the following section, these free-standing thin layers (thickness 3 mm) did not produce large bubbles if the substrate surface was clean. The second system, Fig. 2B, consisted of 1.65 cm-high cylindrical glass vial (inner diameter 5 cm) into which 38 mL solution was poured until the meniscus exceeded the edge of the vial. Special care was taken to avoid solution pouring over the rim of the vial as this seemed to affect the resulting tube dynamics and bubble production. With active tubes, this set-up can produce large oxygen bubbles (see Figs. 2C,D). Moreover, the shape of the large bubble and collective behavior was obtained the same when a cylindrical glass beaker with a slight bend in the brim (diameter = 2.5 cm, height = 3.0 cm) or a polystyrene petri dish (diameter = 3.5 cm, height = 1.2 cm) was used. The deformation of the large bubble was likely related to the surface tension of the solution, not to the substrate edge.

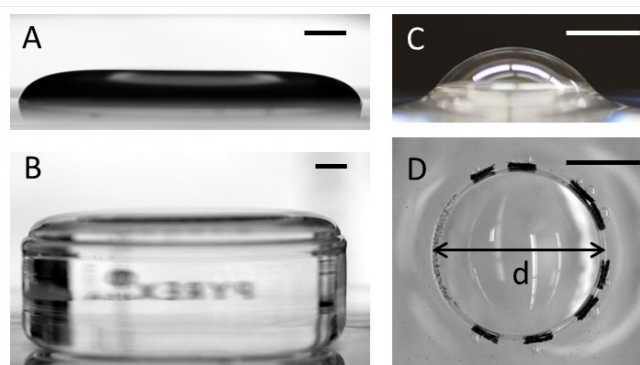


**Fig. 2** (A) Side view of a thin-layer of  $\text{H}_2\text{O}_2$  solution. (B) A cylindrical vial filled with 38 mL  $\text{H}_2\text{O}_2$ . (C,D) Side and top view of the oxygen bubble, respectively. Scale bar: 0.5 cm.

Some reference experiments employed inactive objects of similar shape and size as the active tubes. Just like chemical garden tubes, these rod-like structures were buoyant and positioned themselves underneath the solution-air interface. They were formed by cutting thin wax strings from a hot glue gun (ArtMinds, Mini Glue Sticks; main material: poly(ethylene-vinyl acetate)).

All experiments were performed at 21 °C. Videos and images were acquired with a Nikon D3300 camera (Tamron 90mm f/2.8 macro lens) positioned above the container which was illuminated by diffuse white ceiling light. The acquisition frame rate was 0.33 frames/s for Fig. 1 and 60 frames/s otherwise. The size of the raw images for Fig. 1 was 2992×2000 pixels and 1920×1080 pixels otherwise. Data analysis was performed using in-house MATLAB scripts and Fiji ImageJ software.

## Results and discussion

### Behavior in thin layers

We first describe results obtained from experiments with chemical garden tubes in thin solution layers supported on a hydrophobic polystyrene substrate. A typical example of such a thin layer is shown in Fig. 2A. It has a maximal height of about 3 mm and a rather planar air-solution interface with a steep edge. This system effectively repels the tubes away from the edge, but otherwise creates no strongly preferred position for the micromotors over the large central area of the drop surface.

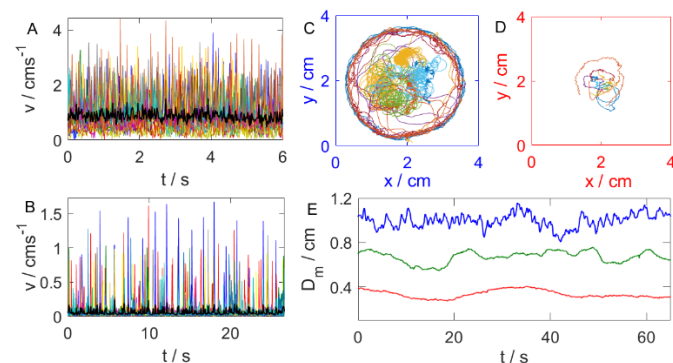


**Fig. 3** (Color online). Behavior of ten chemical garden tubes in a thin layer of 7% H<sub>2</sub>O<sub>2</sub>. (A,B) Tube speeds over short time intervals and (C,D) tube trajectories as measured 15 min and 6.5 h into the experiment, respectively. Different colors correspond to different tubes, and black curves are the average speed of all tubes. (E) Average distance of the tubes from their common center of mass after 15 min (top curve, blue), 3 h (green), and 6.5 h (lowest curve, red).

Figure 3 shows an analysis of a system with ten nearly identical tubes. The velocity data in panels A and B are short time series of the tube speeds obtained 15 min and 6.5 h after the start of the experiment, respectively. All curves consist of spike trains with each spike corresponding to a propulsion event caused by the ejection of an oxygen bubble. The maximal speed during these propulsion events decreases over 6.5 h from about 4 cms<sup>-1</sup> in A to about 1.5 cms<sup>-1</sup> in B. The noisy behavior (black curves) in A,B shows that the speeds of different tubes are uncorrelated, indicating—with respect to this measure—an absence of collective motion. In addition, the average of  $v_a$  decreases from 0.84 cms<sup>-1</sup> to 0.60 mms<sup>-1</sup>.

As shown in Movie S1, the chemical garden tubes can exhibit translational or rotational motion; however, in these thin H<sub>2</sub>O<sub>2</sub> layers, most tubes tend to rotate or spin. The tube trajectories for the early and late situations are shown in Figs. 3C,D, respectively and were collected over a time span of 66.7 s. The data in C indicate preferred locations in a central core disk with a radius of about 1 cm and along a peripheral circle of radius 1.6 cm. Notice that the latter radius is smaller than the radius of the solution edge, which equalled 2.0 cm. Accordingly, the steep edge region of the free-standing layer is effectively a forbidden boundary zone for the buoyant tubes.

For the late dynamics (Fig. 3D), the trajectories are shorter due to the smaller propulsion velocity and the tube ensemble is confined to a smaller area. In a separate experiment, 43 mechanically fatigued tubes in a thin layer of fresh 3% H<sub>2</sub>O<sub>2</sub> solution also aggregated revealing that the confinement behavior is not related to the evaporation of the drop. Nonetheless, we can still distinguish the ring-disk pattern from Fig. 3C, but the rings' radius is now less than 0.7 cm. The origin of the ring-disk pattern in Figs. 3C,D is in large parts caused by the presence of the two tube types that either spin/rotate or trace long arches or nearly linear trajectories. The latter sign responsible for the outer ring, while the rotors tend to stay near the drop center due to buoyancy.

For even later stages ( $\approx 9$  h), tubes aggregated in the central core, but their alignment varied due to jittering self-motion with a low  $\langle v_a \rangle_t = 0.45$  mms<sup>-1</sup>. Interestingly, the small bubbles on the tubes' outer surface restricted the contact among them. Ejected bubbles produce maximal speed of 0.8 cms<sup>-1</sup>, which is sufficiently high to cause tube collisions (Fig. S1). After one day, bubble nucleation as well as self-propulsion had essentially ceased and the tubes settled into a dense cluster with nematic-like alignment and grain boundaries (Fig. S2). In the final equilibrium state, tubes were in close contact.

The tubes' active motion is further analyzed in Fig. 3E where we plot the temporal evolution of the average tube-to-center distance  $D_m$  based on the definition

$$D_m = \frac{1}{n} \sqrt{\sum_{i=1}^n (\vec{s}_i - \vec{s}_m)^2} \quad , \quad (1)$$

where  $n$  is the number of tubes,  $\vec{s}_i$  their position vectors ( $i = 1, \dots, n$ ) and  $\vec{s}_m$  the position of their collective center of mass. This average distance is effectively the swarm radius. The blue (top), green (middle), and red (lowest) curves correspond to time sequences measured 15 min, 3 h, and 6.5 h into the experiment, respectively. During this time span, the swarm radius  $D_m$  drops by a factor of about 2 and its temporal fluctuations decrease in frequency. These changes are the result of diminishing speeds and hence related to the consumption of H<sub>2</sub>O<sub>2</sub> by the catalytic tubes. In addition, the data in E reflect the tubes' tendency to aggregate once the self-propulsion is diminished.

The histograms in Figs. 4A,B show the normalized distribution of the self-propulsion direction (disregarding low tube velocities with  $v < 0.9$  cms<sup>-1</sup>). Panels A and B correspond to early (15 min) and late (6.5 h) behavior, respectively. Both distributions are fairly flat but reveal a mild preference for

motion towards the center of the solution layer ( $\phi=0$ ). The probability ratios for directions with  $\phi \in [0, \pi/2]$  and  $\phi \in [\pi/2, \pi]$  equal 1.47 and 1.35 in A and B, respectively. This preference is clearly the result of a buoyancy-driven motion and weak because the central area of the solution layer is nearly flat. The dominant self-propulsion, however, is isotropic.

Figure 4C shows an example of a near-collision of two active tubes about 3.2 mm away from the center of the solution layer. The two trajectories extend over 0.28 s and are color-coded, representing early and late positions as cyan and purple

propelling tube. Figure 4D shows the tracer speed as a function of its distance to the active tube. From a low maximum of about  $4 \text{ mms}^{-1}$ , the speeds fall off quickly indicating that the interaction has a short-range character and becomes irrelevant for distances larger than about 5 mm. The continuous line is the best fit using the hyperbolic function

$$v = v_0 + \frac{\sigma}{(s - s_0)^\gamma}, \quad (2)$$

where the decay exponent  $\gamma$  equals  $4.16 \pm 0.11$ . The nature of this weak interaction is likely related to the Stokes flow<sup>31</sup> generated by the self-propelled tube as supported by an estimate of the Reynolds number which is below ten.

### Behavior in thick layers

Deeper solution layers tend to result in strong collective dynamics which are self-organized by the repeated formation of a large oxygen bubble. A side view of the system and the bubble are shown in Figs. 2B–D. For this experimental setting, a rhythmic self-assembly of the active micromotors is observed as illustrated by the image sequence in Figs. 5A–E. The first frame (A) of the image sequence depicts a group of six randomly oriented chemical garden tubes. Each of the tubes forms small oxygen bubbles<sup>32</sup> that remain just underneath the air-solution interface and swiftly migrate towards the apex of the meniscus. During and after this motion, the oxygen bubbles merge and rapidly form a large master bubble. This bubble further deforms the solution meniscus and attracts the micromotors via buoyancy forces. The tubes approach the master bubble in a radial direction, but upon arrival align themselves tangentially to the bubble perimeter (B). The resulting bubble-tube complex continues to increase the bubble size (C) until the bubble bursts. This bursting event disperse the tubes (D) and a new aggregation-growth cycle begins (E).

The bubble diameter just before bursting varies from cycle to cycle, but can exceed 1 cm. On the time scale of our experiments, the maximal size increases erratically during the first 15 min. In the later stage ( $t > 15 \text{ min}$ ), due to decomposition of  $\text{H}_2\text{O}_2$  and mechanical fatigue of tubes, the size of the master bubble decreases. We also found that the maximal bubble size (as measured over many cycles) increased with increasing  $\text{H}_2\text{O}_2$  concentration as well as increasing numbers of tubes in the system (see histogram Figs. S3,S4). This stabilization of the growing bubble is possibly related to similar phenomena caused by small particles. For instance, Du et al. reported the stabilization of bubbles by hydrophobic quasi-spherical silica particles<sup>33</sup> and similar phenomena are utilized in particle-stabilized (Pickering) foams<sup>34</sup>.

The growth dynamics of the master bubble are illustrated in Fig. 5F for the example of a system with six tubes. The bubble (as viewed from the top) undergoes slow growth processes followed by rapid bursting rhythmically (see Movie S2). The earliest parts of the growth are not analyzed ( $d < 0.12 \text{ cm}$ ) as an identifiable master bubble has not formed yet and several

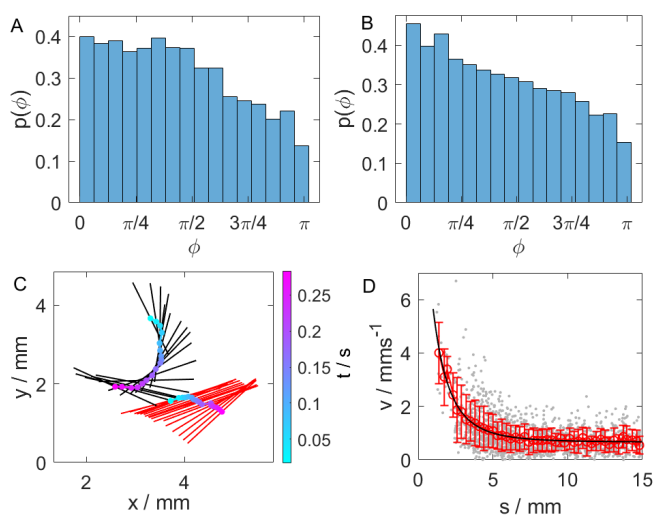


**Fig. 4** (Color online). Tube interaction in a thin layer of 7%  $\text{H}_2\text{O}_2$ . (A,B) Normalized histograms of the active tubes' direction with  $\phi=0$  indicating motion towards the drop center. The distributions are obtained from an early (15 min, A) and late stage (6.5 h, B) of an experiment with ten tubes. (C) Near-collision of two active tubes. The color along the trajectories encodes time, while the black and red lines indicate the motion of the tubes' central axis. (D) Velocity of an inert, buoyant tracer rod (similar size to tube) in the presence of one active tube. The ordinate is the center-to-center distance between the objects. The raw data (gray) are binned and averaged (red, error bars show standard deviations). The continuous (black) line is the best fit to Eq. 2.

segments, respectively. In addition, we show the orientation of the two tubes as black and red lines with lengths equalling the tube lengths. In this example, the tubes were initially on a straight collision course, but avoided a collision by one tube (black lines) performing a nearly 180 degree turn. In this example, the rapid change in direction and orientation occurred within  $\sim 0.1 \text{ s}$  and for a tube-to-tube distance of  $\sim 1 \text{ mm}$ .

The fluid flow created by the active tube causes the repulsion of the nearby tube. To obtain more insights into the range of this interaction, we performed experiments with thin solution layers containing one active chemical garden tube and one inert buoyant tracer (cut from a thin wax string). The size of the rod-shaped tracer was comparable to the size of the self-

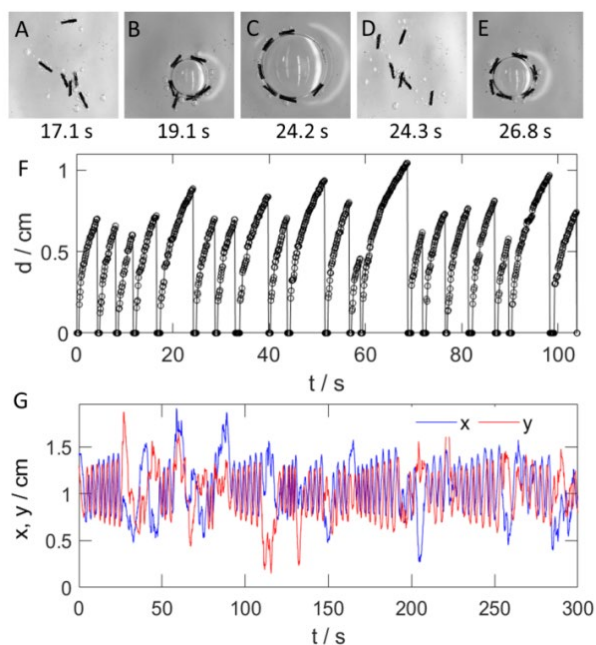


**Fig. 5** (Color online). (A-E) Image sequences illustrating one aggregation-growth cycle. Field of view:  $1.5 \times 1.4 \text{ cm}^2$ . (F) Irregular dynamics of the bubble diameter over several growth-burst cycles using six tubes. (G) Mixed-mode oscillations of the centroid coordinates of a single tube. Concentration: 7%  $\text{H}_2\text{O}_2$ .

smaller bubbles co-exist. Those short unresolved intervals are represented by markers at  $d = 0$ . The data in Fig. 5F give a representative impression of the variation of the maximal bubble size from cycle to cycle and the associated durations. We checked these values for quasiperiodicity and chaotic signatures by constructing return (Poincaré) maps, specifically  $d_{\max}(n+1)$  vs  $d_{\max}(n)$  where  $n$  is the cycle number; however, the resulting plots revealed no patterns and suggested that the variations are random. The shape of the growth branches  $d(t)$  will be discussed later in this Article.

Another aspect of the bubble-tube aggregate is the tubes' tendency to propel along the growing perimeter of the master bubble. Figure 5G shows these dynamics for the case of a single micromotor ( $n = 1$ ) in terms of the tube's centroid coordinates  $x$  and  $y$ . The corresponding graphs feature two repeating types of behavior. The first one is characterized by oscillations caused by the rotation of the tube. Here,  $x$  and  $y$  are phase shifted by 90 degrees and the amplitude increases over time as the bubble grows. This growth also increases the time between maxima due to a constant propulsion speed and an expanding track. The second type of behavior is initiated by the bursting of the bubble and is irregular with the exception of a trend to re-center after the burst-induced repositioning.

We now discuss the growth kinetics of the master bubble and its dependencies on the fuel concentration as well as the number of employed tubes (Fig. 6). For a broad range of

conditions, we find that the growth of the bubble diameter  $d$  was well described by the equation

$$d = \alpha_i(t - t_0)^{\beta_i} \quad , \quad (3)$$

where  $t_0$  is a small parameter accounting for imperfections (1-2 s) in our estimate of the master bubble's nucleation time and  $i$  is used as  $c$  and  $n$  for the  $\text{H}_2\text{O}_2$  concentration and population size, respectively. Accordingly,  $t_0$  has no physical significance.

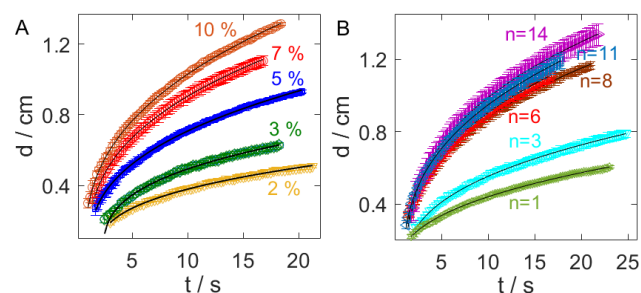


**Fig. 6** (Color online). Temporal evolution of the bubble diameter for different (A)  $\text{H}_2\text{O}_2$  concentrations ( $n = 6$ ) and (B) tube populations (7%  $\text{H}_2\text{O}_2$ ). Black, continuous lines are fits based on Eq. (3).

The black, continuous curves in Fig. 6 are fits based on this equation. Overall fitting yield excellent agreement, although in some cases (e.g. Fig. 6A, 3%), small deviations can be found for early times during which the bubble growth did not yet involve all tubes. Notice that fits were performed for  $d$  and  $t$  in cm and s, respectively.

Figure 7 shows the dependence of the resulting parameters ( $\alpha_c$ ,  $\alpha_n$ ) and ( $\beta_c$ ,  $\beta_n$ ) on the  $\text{H}_2\text{O}_2$  concentration  $c$  and the number of tubes  $n$ . The exponent ( $\beta_c$ ,  $\beta_n$ ) depends neither on the concentration nor on  $n$ . The corresponding averages of  $0.36 \pm 0.02$  (Fig. 7B) and  $0.36 \pm 0.01$  (Fig. 7D) are very close to  $1/3$ , which is the expected value for a constant volume production rate if the expanding bubble has a constant shape. The proportionality parameter  $\alpha_i$  increases with both increasing concentrations and increasing numbers of tubes (Figs. 7A,C). We compared these dependencies to the simple power laws indicated in the figure legends (red curves) and again found very good agreement for fixed exponent of  $1/3$ . The fitting parameters  $c_0$  and  $n_0$  were  $1.21 \pm 0.32\%$  and  $0.41 \pm 0.02$ , respectively. Notice that a—possibly related—concentration threshold of 0.44% had been estimated by two of us in an early study on self-propelled Mn-based chemical garden tubes.<sup>18</sup> This slightly lower value was interpreted as the threshold for directional self-propulsion. Moreover, the  $\alpha_n$  scales as  $n^{\delta_n}$  (see Fig. S5), with an exponent of  $\delta_n = 0.34 \pm 0.03$  validating that  $n_0$  is very close to the expected value of zero. Overall these dependencies of the bubble volume on  $c$ ,  $n$ , and  $t$  suggest the following simple relation for the diameter of a master bubble formed at  $t=0$

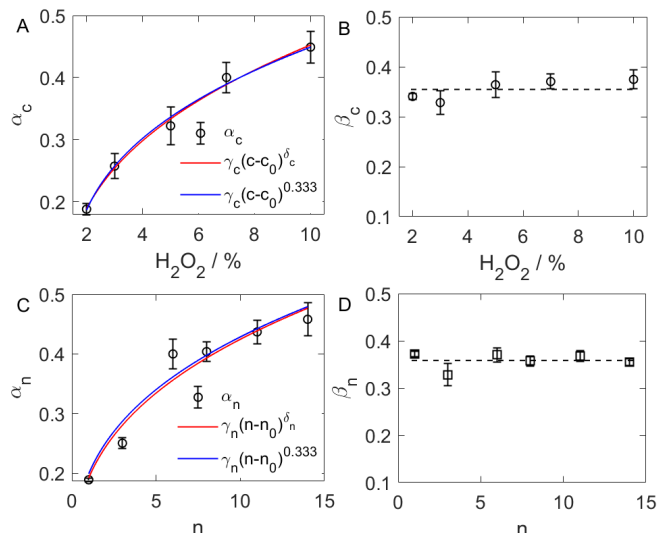


**Fig. 7** (Color online). Bubble growth proportionality parameters ( $\alpha_c$  and  $\alpha_n$ ) and scaling exponents ( $\beta_c$  and  $\beta_n$ ) as a function of (A,B) hydrogen peroxide concentrations and (C,D) number of tubes  $n$ . The floating exponents  $\delta_c$  and  $\delta_n$  (red curves in A,C) were  $0.36 \pm 0.06$  and  $0.30 \pm 0.03$ , respectively.

$$d \propto [n(c - c_0)t]^{1/3} \quad (4)$$

For the investigated range of experimental parameters, this equation quantifies the intuitive trend of faster bubble growth in the presence of additional tubes and higher fuel concentrations. We also reemphasize that all master bubbles eventually burst (maximal observed diameter: 2.18 cm), which creates an obvious limit for the long-term applicability of eq. (4).

Lastly, we analyze the tube swarm's degree of order, which rhythmically varies between a dispersed (disordered) and a bubble-bound (ordered) state. For these analyses, we first measured the distance of each tube's centroid from the swarm center and then computed the corresponding standard deviation  $\sigma$  as a function of time (blue traces in Fig. 8). This standard deviation is zero in the perfectly ordered state (tubes tangentially aligned around master bubble) and large in the dispersed state.

In addition, we calculated the orientation of each tube with respect to the swarm center so that tubes positioned tangentially to the edge of the master bubble registered with an angle  $\theta$  of close to  $90^\circ$ , whereas radially approaching (and dispersing) tubes corresponded to  $0^\circ$ . From the cosine of these angles, we then computed the standard deviation  $\sigma_{|\cos\theta|}$  which is close to zero in the ordered state and high in the dispersed state (red curves in Fig. 8).

The ordered-unordered states are investigated for different concentrations and tube population. Figures 8A and 8B illustrate the examples of six tubes and  $H_2O_2$  concentrations of 7% and 2%, respectively, and Fig. 8C indicates the collective behavior of 11 tubes for 7%  $H_2O_2$ . High concentrations of

hydrogen peroxide enhance the propulsion activities, which increases their tendency to move away from each other.

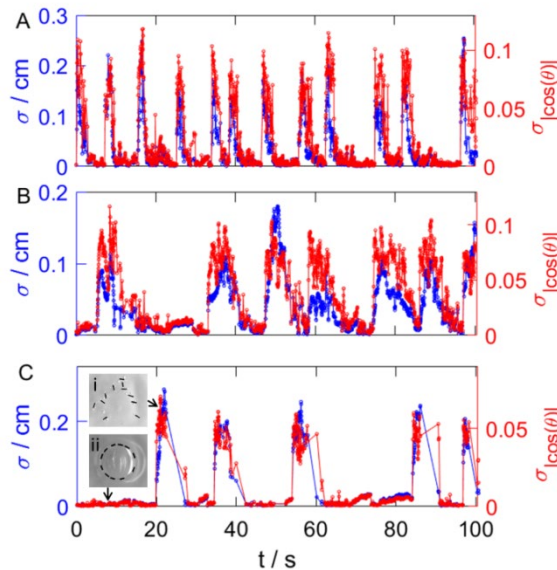


**Fig. 8** (Color online). Order-disorder transitions as monitored by the standard deviation of the distribution of the tube distances from the swarm center  $\sigma$  and the tube orientations  $\sigma_{|\cos\theta|}$ . The number of tubes and the  $H_2O_2$  concentrations were: (A)  $n = 6$ , 7%, (B)  $n = 6$ , 2%, and (C)  $n = 11$ , 7%. The images in (C) illustrate the (i) disordered and (ii) ordered state of the tubes. Field of view:  $2.0 \times 1.8 \text{ cm}^2$ .

However, increasing the  $H_2O_2$  concentration and tube population also increases the maximal diameter of the master bubble and its growth rate. Interestingly, the master bubble size reaches the cm-scale, which assists the tubes in establishing their preferred tangential orientation to the less curved bubble edge. The capillary force stabilizes the tubes under which they maintain the convoy-like head-to-tail arrangement (Fig. 8C(ii)). Figures 8A-8C show that in all the cases,  $\sigma$  and  $\sigma_{|\cos\theta|}$  are well matched, indicating a good correlation between the tubes' orientation and the distances with respect to the swarm center.

## Conclusions

In summary, we have shown that self-propelling chemical garden tubes can form swarm-like collectives with either mild or strong forms of interaction. Mild interactions were observed in thin layers and resulted from collision-like events and also weak fluid motion around the moving tubes. Strong interaction is tightly linked to forming a large master bubble that attracts and aligns the tubes. We note that possibly related behavior was observed by Solovov et al. for Ti/Cr/Pt microtubes produced by rolled-up nanosheets.<sup>35</sup> In our experiments, the lifetime of the master bubble increased with the number of employed chemical garden tubes, and for sufficiently long-lived ordered states could also induce a

convoy-like revolving motion of the tubes along the perimeter of the expanding bubble.

Future studies could extend our work to systems containing surfactants and two immiscible liquid that potentially further increase the lifetime of the master bubble. For a thin (non-aqueous) top layer bound by a solid surface, this should yield stable master bubbles and possibly additional levels of interaction if these large bubbles coalesce or pack into ordered patterns. Another interesting direction for future investigations is the use of the oxygen bubble as localized, high concentration units for oxygen-dependent reactions. Such processes could set-up a steady state between oxygen production and consumption and manufacture localized product domains as well as complex product patterns. Moreover, the control of collective behavior can be explored by self-organized paramagnetic tubes<sup>36</sup>.

## Author Contributions

Pawan Kumar: conceptualization, formal analysis, investigation, writing – review & editing Qingpu Wang: conceptualization, methodology, writing – review & editing Dezső Horváth and Ágota Tóth: validation, writing – review & editing Oliver Steinbock: conceptualization, funding acquisition, writing – original draft, review & editing.

## Conflicts of interest

There are no conflicts to declare.

## Acknowledgements

This material is based upon work supported by the National Science Foundation under grant No. 1609495.

## Notes and references

‡ Footnotes relating to the main text should appear here. These might include comments relevant not central to the matter under discussion, limited experimental and spectral data, and crystallographic data.

§  
§§

1. B. C. Batista, P. Cruz and O. Steinbock, *Langmuir*, 2014, **30**, 9123-9129.
2. J. H. E. Cartwright, J. M. García-Ruiz, M.L Novella and F. Otálora, *J. Colloid Interface Sci.*, 2002, **256**, 351-359.
3. S. Thouvenel-Romans and O. Steinbock, *J. Am. Chem. Soc.*, 2003, **125**, 4338-4341.
4. J. H. E. Cartwright, B. Escribano, S. Khokhlov and C. I. Sainz-Díaz, *Phys. Chem. Chem. Phys.*, 2011, **13**, 1030-1036.
5. J. Pantaleone, A. Toth, D. Horvath, J. R. McMahan, R. Smith, D. Butki, J. Braden, E. Mathews, H. Geri and J. Maselko, *Phys. Rev. E*, 2008, **77**, 046207.

6. S. S. S. Cardoso, J. H. E. Cartwright and C. I. Sainz-Díaz, *ICARUS*, 2019, **319**, 337-348.
7. M. Emmanuel, E. Lantos, D. Horváth and Á. Tóth, *Soft Matter*, 2022, **18**, 1731-1736.
8. L. M. Barge, I. J. Doloboff, L. M. White, G. D. Stucky, M. J. Russell and I. Kanik, *Langmuir*, 2012, **28**, 3714-3721.
9. E. A. B. Hughes, R. L. Williams, S. C. Cox and L. M. Grover, *Langmuir*, 2017, **33**, 2059-2067.
10. G. J. T. Cooper, R. W. Bowman, E. P. Magennis, F. Fernandez-Trillo, C. Alexander, M. J. Padgett and L. Cronin, *Angew. Chem. Int. Ed.*, 2012, **51**, 12754-12758.
11. L. J. Points, G. J. T. Cooper, A. Dolbecq, P. Mialane and L. Cronin, *Chem. Commun.*, 2016, **52**, 1911-1914.
12. P. Kumar, D. Horváth and Á. Tóth, *Soft Matter*, 2020, **16**, 8325-8329.
13. L. Zhu, C. Fu Tan, M. Gao and G. W. Ho, *Adv. Mater.*, 2015, **27**, 7713-7719.
14. R. Makki, X. Ji, H. Mattoussi and O. Steinbock, *J. Am. Chem. Soc.*, 2014, **136**, 6463-6469.
15. E. A. B. Hughes, M. Chipara, T. J. Hall, R. L. Williams and L. M. Grover, *Biomater. Sci.*, 2020, **8**, 812-822.
16. L. M. Barge and L. M. White, *Astrobiology*, 2017, **17**, 820-833.
17. L. M. Barge, Y. Abedian, M. J. Russell, I. J. Doloboff, J. H. E. Cartwright, R. D. Kidd and I. Kanik, *Angew. Chem. Int. Ed.*, 2015, **54**, 8184-8187.
18. Q. Wang, P. Knoll and O. Steinbock, *J. Phys. Chem. B*, 2021, **125**, 51, 13908-13915.
19. Y. Mei, G. Huang, A. A. Solovev, E. B. Ureña, I. Mönch, F. Ding, T. Reindl, R. K. Y. Fu, P. K. Chu and O. G. Schmidt, *Adv. Mater.*, 2008, **20**, 4085-4090.
20. R. J. Archer, A. J. Parnell, A. I. Campbell, J. R. Howse and S. J. Ebbens, *Adv. Sci.*, 2018, **5**, 1700528.
21. W. Liu, H. Ge, Z. Gu, X. Lu, J. Li and J. Wang, *Small*, 2018, **14**, 1802771.
22. T. Li, L. Li, W. Song, L. Wang, G. Shao and G. Zhang, *ECS J. Solid State Sci. Technol.*, 2015, **4**, S3016.
23. M. Urso, C. Iffelsberger, C. C. Mayorga-Martinez and M. Pumera, *Small Methods*, 2021, **5**, 2100511.
24. Q. Wang and O. Steinbock – submitted.
25. M. A. Bees, *Ann. Rev. Fluid Mech.*, 2020, **52**, 449-476.
26. R. Ni and N. T. Ouelette, *Phys. Biol.*, 2016, **13**, 045002.
27. T. Vicsek and A. Zafeiris, *Phys. Rep.*, 2012, **517**, 71-140.
28. M. Moussaïd, D. Helbing and G. Theraulaz, *Proc. Natl. Acad. Sci. USA*, 2011, **108**, 6884-6888.
29. M. Ibele, T. E. Mallouk and A. Sen, *Angew. Chem. Int. Ed.*, 2009, **121**, 3358-3362.
30. D. Jin, J. Yu, K. Yuan and L. Zhang, *ACS Nano*, 2019, **13**, 5, 5999-6007.
31. H. Lamb, *Hydrodynamics*, 6th ed.; Dover: New York.
32. S. Nakata, M. Nomura, H. Yamamoto, S. Izumi, N. J. Suematsu, Y. Ikura and T. Amemiya, *Angew. Chem. Int. Ed.*, 2017, **129**, 879-882.
33. Z. Du, M. P. Bilbao-Montoya, B. P. Binks, E. Dickinson, R. Ettelaie and B. S. Murray, *Langmuir*, 2003, **19**, 3106-3108.
34. S. Fujii and Y. Nakamura, *Langmuir*, 2017, **33**, 7365-7379.
35. A. A. Solovev, Y. Mei and O. G. Schmidt, *Adv. Mater.*, 2010, **22**, 4340-4344.
36. D. Takács, G. Schuszter, D. Sebők, Á. Kukovecz, D. Horváth and Á. Tóth, *Chem. Eur. J.*, 2019, **25**, 14826-14833.